

Staggered \mathcal{PT} -symmetric ladders with cubic nonlinearity

Jennie D'Ambroise,¹ P. G. Kevrekidis,² and Boris A. Malomed³

¹*Department of Mathematics and Statistics, Amherst College, Amherst, MA 01002-5000, USA*

²*Department of Mathematics and Statistics, University of Massachusetts, Amherst, MA 01003-9305, USA*

³*Department of Physical Electronics, School of Electrical Engineering, Faculty of Engineering, Tel Aviv University, Tel Aviv 69978, Israel*

We introduce a ladder-shaped chain with each rung carrying a \mathcal{PT} -symmetric gain-loss dimer. The polarity of the dimers is *staggered* along the chain, meaning alternation of gain-loss and loss-gain rungs. This structure, which can be implemented as an optical waveguide array, is the simplest one which renders the system \mathcal{PT} -symmetric in both horizontal and vertical directions. The system is governed by a pair of linearly coupled discrete nonlinear Schrödinger (DNLS) equations with self-focusing or defocusing cubic onsite nonlinearity. Starting from the analytically tractable anti-continuum limit of uncoupled rungs and using the Newton's method for continuation of the solutions with the increase of the inter-rung coupling, we construct families of \mathcal{PT} -symmetric discrete solitons and identify their stability regions. Waveforms stemming from a single excited rung and double ones are identified. Dynamics of unstable solitons is investigated too.

PACS numbers: 05.45.-a, 63.20.Ry

I. INTRODUCTION

A vast research area, often called discrete nonlinear optics deals with evanescently coupled arrayed waveguides featuring material nonlinearity [1]. Discrete arrays of optical waveguides have drawn a great deal of interest not only because they introduce a vast phenomenology of the nonlinear light propagation, such as e.g. the prediction [2] and experimental creation [3] of discrete vortex solitons, but also due to the fact that they offer a unique platform for emulating the transmission of electric signals in solid-state devices, which is obviously interesting for both fundamental studies and applications [1, 4]. Furthermore, the flexibility of techniques used for the creation of virtual (photoinduced) [5] and permanently written [6] guiding arrays enables the exploration of effects which can be difficult to directly observe in other physical settings, such as Anderson localization [7].

Another field in which arrays of quasi-discrete waveguides find a natural application is the realization of the optical \mathcal{PT} (parity-time) symmetry [8]. On the one hand, a pair of coupled nonlinear waveguides, which carry mutually balanced gain and loss, make it possible to realize \mathcal{PT} -symmetric spatial or temporal solitons (if the waveguides are planar ones or fibers, respectively), which admit an exact analytical solution, including their stability analysis [9]. On the other hand, a \mathcal{PT} -symmetric dimer, i.e., the balanced pair of gain and loss nodes, can be embedded, as a defect, into a regular guiding array, with the objective to study the scattering of incident waves on the dimer [10, 11, 13]. We note here in passing that some times, also the term “dipoles” may be used for describing such dimers, however we will not make use of it here, to avoid an overlap in terminology with classical dipoles in electrodynamics as discussed e.g. in [12]. Discrete solitons pinned to a nonlinear \mathcal{PT} -symmetric defect have been reported too [13]. Such systems, although governed by discrete nonlinear Schrödinger (DNLS) equa-

tions corresponding to non-Hermitian Hamiltonians, may generate real eigenvalue spectra (at the linear level), provided that the gain-loss strength does not exceed a critical value, above which the \mathcal{PT} symmetry is broken [14] [self-defocusing nonlinearity with the local strength growing, in a one-dimensional (1D) system, from the center to periphery at any rate faster than the distance from the center, gives rise to stable fundamental and higher-order solitons with *unbreakable* \mathcal{PT} -symmetry [15]].

One- and two-dimensional (1D and 2D) lattices, built of \mathcal{PT} dimers, were introduced in Refs. [16, 17] and [18], respectively. Discrete solitons, both quiescent and moving ones, were found in these systems [16, 18]. In the continuum limit, those solitons go over into those in the above-mentioned \mathcal{PT} -symmetric coupler [9]. Accordingly, a part of the soliton family is stable, and another part is unstable. Pairs of parallel and anti-parallel coupled dimers, in the form of \mathcal{PT} -symmetric plaquettes (which may be further used as building blocks for 2D chains) were investigated too [19, 20].

The objective of the present work is to introduce a *staggered* chain of \mathcal{PT} -symmetric dimers, with the orientations of the dimers alternating between adjacent sites of the chain. This can also be thought of as an extension of a plaquette from Refs. [19, 20] towards a lattice. While this ladder-structured lattice is not a full 2D one, it belongs to a class of chain systems which may be considered as 1.5D models [21].

As shown in Section II, where the model is introduced, the fundamental difference from the previously studied ones is the fact that such a system, although being nearly one-dimensional, actually realizes the \mathcal{PT} symmetry in the 2D form, with respect to both horizontal and vertical directions. In Section III we start the analysis from the solvable anti-continuum limit (ACL) [22], in which the rungs of the ladder are uncoupled (in the opposite continuum limit, the ladder degenerates into a single NLS equation). Using parametric continuation from this limit

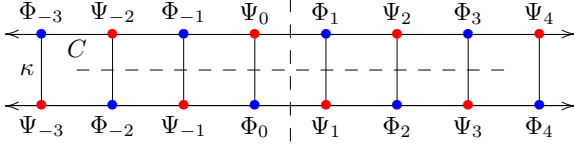


FIG. 1: (Color online) The staggered ladder-shaped lattice with horizontal (C) and vertical (κ) coupling constants. Red and blue dots designate sites carrying the mutually balanced gain and loss, respectively. The dashed lines designate the horizontal and vertical axes of the \mathcal{PT} symmetry.

makes it possible to construct families of discrete solitons in a numerical form. Such solution branches are initiated, in the ACL, by a single excited rung, as well as by the excitation confined to several rungs. The soliton stability is systematically analyzed in Section III too and, if the modes are identified as unstable, their evolution is examined to observe the instability development. The paper is concluded by Section IV, where also some directions for future study are presented.

II. THE MODEL

We consider the ladder configuration governed by the DNLS system with intersite coupling constant C ,

$$\begin{aligned} i\frac{d\Psi_n}{dt} + \frac{C}{2}(\Phi_{n+1} + \Phi_{n-1} - 2\Psi_n) \\ + \sigma|\Psi_n|^2\Psi_n = i\gamma\Psi_n - \kappa\Phi_n, \\ i\frac{d\Phi_n}{dt} + \frac{C}{2}(\Psi_{n+1} + \Psi_{n-1} - 2\Phi_n) \\ + \sigma|\Phi_n|^2\Phi_n = -i\gamma\Phi_n - \kappa\Psi_n, \end{aligned} \quad (1)$$

where evolution variable t is the propagation distance, in terms of the optical realization. Coefficients $+i\gamma$ and $-i\gamma$ with $\gamma > 0$ represent \mathcal{PT} -symmetric gain-loss dimers, whose orientation is staggered (alternates) along the ladder, the sites carrying gain and loss being represented by amplitudes $\Psi_n(t)$ and $\Phi_n(t)$, respectively. Cubic nonlinearity with coefficient σ is present at every site, and $\kappa > 0$ accounts for the vertical coupling along the ladder's rungs, each representing a \mathcal{PT} -symmetric dimer. The system is displayed in Fig. 1. As seen in the figure, the nearly 1D ladder realizes the \mathcal{PT} symmetry in the 2D form, with respect to the horizontal axis, running between the top and bottom strings, and, simultaneously, with respect to any vertical axis drawn between adjacent rungs.

By means of obvious rescaling, we can fix $|\sigma| = 1$, hence the nonlinearity coefficient takes only two distinct values, which correspond, respectively, to the self-focusing and defocusing onsite nonlinearity, $\sigma = +1$ and $\sigma = -1$. The usual DNLS equation admits the sign reversal of σ by means of the well-known staggering transformation [22]. However, once we fix $\gamma > 0$ (and also

$\kappa > 0$) in Eq. (1), this transformation cannot be applied, as it would also invert the signs of γ and κ .

The single self-consistent continuum limit of system (1), corresponding to $C \rightarrow \infty$, is possible for the fields related by $\Phi = e^{i\delta}\Psi$, with phase shift $\delta = \gamma/C$. Replacing, in this limit, the finite-difference derivative by the one with respect to the continuous coordinate, $x \equiv n/\sqrt{C}$, yields the standard NLS equation,

$$i\frac{\partial\Psi}{\partial t} + \frac{1}{2}\frac{\partial^2\Psi}{\partial x^2} + \sigma|\Psi|^2\Psi = -\kappa\Psi. \quad (2)$$

Given its ‘‘standard’’ nature, leading to a full mutual cancellation of the gain and loss terms, we will not pursue this limit further. Instead, as shown below, we will use as a natural starting point for examining nontrivial localized modes in the discrete system (1) the opposite ACL, which corresponds to $C \rightarrow 0$, i.e., the set of uncoupled rungs.

Stationary solutions to Eqs. (1) with real propagation constant Λ are sought in the usual form, $\Psi_n = e^{i\Lambda t}u_n$ and $\Phi_n = e^{i\Lambda t}v_n$, where functions u_n and v_n obey the stationary equations,

$$\begin{aligned} -\Lambda u_n + \frac{C}{2}(v_{n+1} + v_{n-1} - 2u_n) \\ + \sigma|u_n|^2u_n = i\gamma u_n - \kappa v_n, \\ -\Lambda v_n + \frac{C}{2}(u_{n+1} + u_{n-1} - 2v_n) \\ + \sigma|v_n|^2v_n = -i\gamma v_n - \kappa u_n. \end{aligned} \quad (3)$$

Numerical solutions of these equations for discrete solitons are produced in the next section. To analyze the stability of the solutions, we add perturbations with an infinitesimal amplitude ε and frequencies ω ,

$$\begin{aligned} \Psi_n(t) &= (u_n + \varepsilon(a_n e^{i\omega t} + b_n e^{-i\omega^* t}))e^{i\Lambda t}, \\ \Phi_n(t) &= (v_n + \varepsilon(c_n e^{i\omega t} + d_n e^{-i\omega^* t}))e^{i\Lambda t}. \end{aligned} \quad (4)$$

The linearization of Eq. (1) with respect to the small perturbations leads to the eigenvalue problem,

$$M \begin{bmatrix} a_n \\ b_n^* \\ c_n \\ d_n^* \end{bmatrix} = \omega \begin{bmatrix} a_n \\ b_n^* \\ c_n \\ d_n^* \end{bmatrix}, \quad (5)$$

where M is a $4N \times 4N$ matrix for the ladder of length N . Using standard indexing, $N \times N$ submatrices of M are defined as

$$\begin{aligned} M_{11} &= \text{diag}(p_n^* - \Lambda - C), \\ M_{22} &= \text{diag}(\Lambda + C - p_n), \\ M_{33} &= \text{diag}(q_n - \Lambda - C), \\ M_{44} &= \text{diag}(\Lambda + C - q_n^*), \\ M_{12} &= -M_{21}^* = \text{diag}(\sigma u_n^2), \\ M_{34} &= -M_{43}^* = \text{diag}(\sigma v_n^2), \\ M_{13} &= M_{31} = -M_{24} = -M_{42} = \frac{C}{2}G + \text{diag}(\kappa), \end{aligned} \quad (6)$$

$$\begin{aligned} p_n &\equiv i\gamma + 2\sigma|u_n|^2, \\ q_n &\equiv i\gamma + 2\sigma|v_n|^2, \end{aligned} \quad (7)$$

where G is an $N \times N$ matrix of zero elements, except for the super- and sub-diagonals that contain all ones.

For the zero solution of the stationary equation (3), $u_n = v_n = 0$, matrix M has constant coefficients, hence perturbation eigenmodes can be sought for as $a_n = Ae^{ikn}$, $b_n = 0$, $c_n = Be^{ikn}$, $d_n = 0$. Then Eq. (5) becomes a 2×2 system, whose eigenvalues can be found explicitly:

$$\omega = -(\Lambda + C) \pm \sqrt{(C \cos k + \kappa)^2 - \gamma^2}, \quad (8)$$

so that ω is real only for $C \leq \kappa - \gamma$. In other words, the \mathcal{PT} -symmetry is broken, with $i\omega$ acquiring a positive real part, which drives the exponential growth of the perturbations, at

$$\gamma > \gamma_{\text{cr}}^{(1)}(C) \equiv \kappa - C. \quad (9)$$

It is interesting to observe here that the coupling between the rungs decreases the size of the interval of the unbroken \mathcal{PT} -symmetry of the single dimer [8, 14].

In the stability region, Eq. (8) demonstrates that real perturbation frequencies take values in the following intervals:

$$\begin{aligned} -(\Lambda + C) - \sqrt{(\kappa + C)^2 - \gamma^2} &< \omega < \\ &-(\Lambda + C) - \sqrt{(\kappa - C)^2 - \gamma^2}, \\ -(\Lambda + C) + \sqrt{(\kappa - C)^2 - \gamma^2} &< \omega < \\ &-(\Lambda + C) + \sqrt{(\kappa + C)^2 - \gamma^2}. \end{aligned} \quad (10)$$

Similarly, for the perturbations in the form of $a_n = 0$, $b_n = Ae^{ikn}$, $c_n = 0$, $d_n = Be^{ikn}$ the negatives of expressions (8) are also eigenvalues of the zero stationary solution, and at $\gamma < \gamma_{\text{cr}}^{(1)}(C)$, they fall into the negatives of intervals (10).

Simultaneously, Eq. (8) and its negative counterpart give the dispersion relation for plane waves (“phonons”) in the linearized version of Eq. (1). Accordingly, intervals (10), along with their negative counterparts, represent phonon bands of the linearized system.

In Section III we produce stationary solutions in the form of discrete solitons. This computation begins by finding exact solutions for the ACL, $C = 0$, and then the continuing the solutions numerically to $C > 0$, by means of the Newton’s method for each C (i.e., utilizing the converging solution obtained for a previous value of C as an initial seed for the Newton’s algorithm with $C \rightarrow C + \Delta C$). As suggested by Eq. (9), we restrict the analysis to $0 < \gamma \leq \kappa$, so as to remain within the \mathcal{PT} -symmetric region at $C = 0$. Subsequently, the stability interval of the so constructed solutions is identified, in a numerical form too.

III. DISCRETE SOLITONS AND THEIR STABILITY

A. The anti-continuum limit (ACL), $C = 0$

To construct stationary localized solutions of Eqs. (1) at $C = 0$, when individual rungs are decoupled, we substitute

$$u_n = e^{i\delta_n} v_n \quad (11)$$

with real δ_n in Eq. (3), which yields relations

$$\gamma = -\kappa \sin \delta_n, \quad \sigma|v_n|^2 = -\kappa \cos \delta_n + \Lambda. \quad (12)$$

For the uncoupled ladder, one can specify either a single-rung solution, with fields at all sites set equal to zero except for u_1 satisfying Eq. (12), or a double-rung solution with nonzero fields u_1 and u_2 satisfying the same equations. We focus on these two possibilities in the ACL (although larger-size solutions are obviously possible too). These are the direct counterparts of the single-node and two-node solutions that have been extensively studied in 1D and 2D DNLS models [22].

We take parameters satisfying constraints

$$\sigma > 0, \quad \Lambda > \kappa, \quad (13)$$

to make the second equation (12) self-consistent. Then, two solution branches for δ_n are possible. The first branch satisfies $-\pi/2 \leq \delta_{\text{in}} \equiv \arcsin(-\gamma/\kappa) \leq 0$ and $\cos(\delta_{\text{in}}) \geq 0$. Choosing a solution with $\delta_n = \delta_{\text{in}}$ in the rung carrying nonzero fields, we name it an *in-phase rung*, as the phase shift between the gain and loss poles of the respective dimer is smaller than $\pi/2$, namely, $|\arg(vu^*)| \in [0, \pi/2]$. The second branch satisfies $-\pi \leq \delta_{\text{out}} \equiv -\pi + |\delta_{\text{in}}| \leq -\pi/2$ and $\cos \delta_{\text{out}} \leq 0$. The rung carrying the solution with $\delta_n = \delta_{\text{out}}$ is called an *out-of-phase* one, as the respective phase shift between the elements exceeds $\pi/2$, viz., $|\arg(vu^*)| \in [\pi/2, \pi]$. The two branches meet and disappear at $\gamma = \kappa$, when $\delta_{\text{in}} = \delta_{\text{out}} = -\pi/2$. Recall that $\gamma = \kappa = \gamma_{\text{cr}}^{(1)}(C = 0)$ [see Eq. (9)] is the boundary of the \mathcal{PT} -symmetric region for $C = 0$. These branches can be also be considered as stemming from the Hamiltonian limit of $\gamma = 0$, where $\delta_{\text{in}} = 0$ and $\delta_{\text{out}} = \pi$ correspond, respectively, to the usual definitions of the in- and out-of-phase Hamiltonian dimers.

The stability eigenfrequencies for stationary solitons at $C = 0$ can be readily calculated analytically in the ACL [14]. In this case, M has the same eigenvalues as submatrices

$$m_0 = \begin{pmatrix} -\Lambda - i\gamma & 0 & \kappa & 0 \\ 0 & \Lambda - i\gamma & 0 & -\kappa \\ \kappa & 0 & -\Lambda + i\gamma & 0 \\ 0 & -\kappa & 0 & \Lambda + i\gamma \end{pmatrix},$$

which is associated with zero-amplitude (unexcited)

rungs, and

$$m_n = \begin{pmatrix} -\Lambda + p_n^* & \sigma u_n^2 & \kappa & 0 \\ -\sigma(u_n^*)^2 & \Lambda - p_n & 0 & -\kappa \\ \kappa & 0 & -\Lambda + q_n & \sigma v_n^2 \\ 0 & -\kappa & -\sigma(v_n^*)^2 & \Lambda - q_n^* \end{pmatrix},$$

associated with the excited ones, which carry nonzero stationary fields, with v_n, u_n taken as per Eqs. (11) and (12). In other words, each of the four eigenvalues of m_0 ,

$$\omega = \pm\Lambda \pm \sqrt{\kappa^2 - \gamma^2}, \quad (14)$$

is an eigenvalue of M with multiplicity equal to the number of zero-amplitude rungs, while each of the four eigenvalues of m_n ,

$$\omega = \pm 0, \pm 2\Lambda\sqrt{2\alpha_*^2 - \alpha_*}, \quad (15)$$

appears as an eigenvalue of M with multiplicity equal to the number of excited rungs. Here $\alpha_* = \alpha_{\text{in}} = \kappa \cos(\delta_{\text{in}})/\Lambda \equiv \sqrt{(\kappa^2 - \gamma^2)/\Lambda^2}$, and $\alpha_* = \alpha_{\text{out}} = \kappa \cos(\delta_{\text{out}})/\Lambda \equiv -\sqrt{(\kappa^2 - \gamma^2)/\Lambda^2}$ for an in- and out-of-phase rung, respectively.

Equation (15) shows that the out-of-phase excited rung is always stable, as it has $\text{Re}(i\omega) = 0$. Similarly, the in-phase excited rung is stable for $\kappa^2 - \gamma^2 \geq \Lambda^2/4$, and unstable for $0 < \kappa^2 - \gamma^2 < \Lambda^2/4$. Thus, for solutions that contain an excited in-phase rung in the initial configuration at $C = 0$, there are the two critical values, *viz.*, $\gamma_{\text{cr}}^{(1)}(C = 0) = \kappa$ given by Eq. (9), and the additional one, which designates the instability area for the uncoupled in-phase rungs:

$$\gamma > \gamma_{\text{cr}}^{(2)}(C = 0) = \sqrt{\kappa^2 - \Lambda^2/4}. \quad (16)$$

A choice alternative to Eq. (13) is

$$\sigma < 0, \Lambda < -\kappa. \quad (17)$$

In this case, the analysis differs only in that the sign of α_* in Eq. (15) is switched. That is, the in-phase rung is now associated to negative $\alpha_* = \alpha_{\text{in}} = \kappa \cos(\delta_{\text{in}})/\Lambda = -\sqrt{(\kappa^2 - \gamma^2)/\Lambda^2}$, while the out-of-phase one to positive $\alpha_* = \alpha_{\text{out}} = \kappa \cos(\delta_{\text{out}})/\Lambda \equiv \sqrt{(\kappa^2 - \gamma^2)/\Lambda^2}$. In this case, the in-phase rung is always stable, while its out-of-phase counterpart is unstable at $\gamma > \gamma_{\text{cr}}^{(2)}(C = 0)$, see Eq. (16).

B. Discrete solitons at $C > 0$

To construct soliton solutions for coupling constant C increasing in steps of ΔC , we write Eq. (3) as a system of $4N$ equations for $4N$ real unknowns w_n, x_n, y_n, z_n , with $u_n \equiv w_n + ix_n$, $v_n \equiv y_n + iz_n$. Then we apply the Newton's method with the initial guess at each step taken as the soliton solution found at the previous value of C , as mentioned above. Thus, the initial guess at $C = \Delta C$

is the analytical solution for $C = 0$ given by Eqs. (11)-(12) with parameters taken according to either Eq. (13) or Eq. (17).

Figure 2 shows $|u_n|^2$ for the solutions identified by this process on a (base 10) logarithmic scale as a function of C for parameters taken as per Eq. (13). The logarithmic scale is chosen, as it yields a clearer picture of the variation of the solution's spatial width, as C varies. The different solutions displayed in Fig. 2 include those seeded by the single excited in- and out-of-phase rungs (the top row), and two-rung excitations for which there are three possibilities: in- in both and out-of-phase structures in both rungs (the second row), as well as a mixed structure involving one rung initially excited in-phase, and the other one excited out-of-phase (the bottom row). In Figure 3 we plot $|u_n|^2$ for fixed C across the various configurations. A point that is clearly illustrated by this figure, which is not evident on the logarithmic scale of Fig. 2, is the asymmetric spatial structure of the mixed-phase solution of the bottom row (asymmetric solitary waves have also been proposed in full 2D lattices [23]; see also the detailed analysis of [22]). Equations (11)-(12) show that, for $C = 0$, since the out-of-phase case corresponds to $\cos(\delta_{\text{out}}) \leq 0$, the amplitude of the out-of-phase rung, $|v_n| = |u_n|$, with $\sigma = +1$, is larger in comparison with its in-phase counterpart, which has $\cos(\delta_{\text{in}}) \geq 0$. The asymmetry for the mixed-phase solution persists for $C > 0$, Fig. 3 showing an example of this. Then, Fig. 4 shows more explicitly the increasing width of the soliton, using the second moment of the density distribution, as the respective diagnostic,

$$w(C) \equiv \sqrt{\frac{\sum_n n^2 |u_n|^2}{\sum_n |u_n|^2}}, \quad (18)$$

versus C for the solutions shown in Fig. 2. It is relevant to point out that the variation of this width-measuring quantity is fairly weak in the case of the out-of-phase solutions and mixed ones, while it is more significant in the case of the single and double in-phase excited rungs.

In Fig. 5 the absolute value of the phase difference between fields u_n and v_n at two sides of the ladder is shown. In other words, this figure shows whether each rung of the ladder belongs to the in-phase or out-of-phase type, as a function of C . This figure reveals that, as C increases, there is a progressive spatial expansion (across n) in the number of sites supporting a phase difference that develops around the initially excited sites. The individual phases of u_n and v_n are shown in Fig. 6. We show in the bottom two plots of Fig. 6 that two different types of phase profiles can arise; one type has phase with the same sign on both the left and right sides of the outer portion of the ladder, and the second type has phases that are of opposite sign on the left and right sides of the outer portion of the ladder. We address this point more in the next section where we discuss stability.

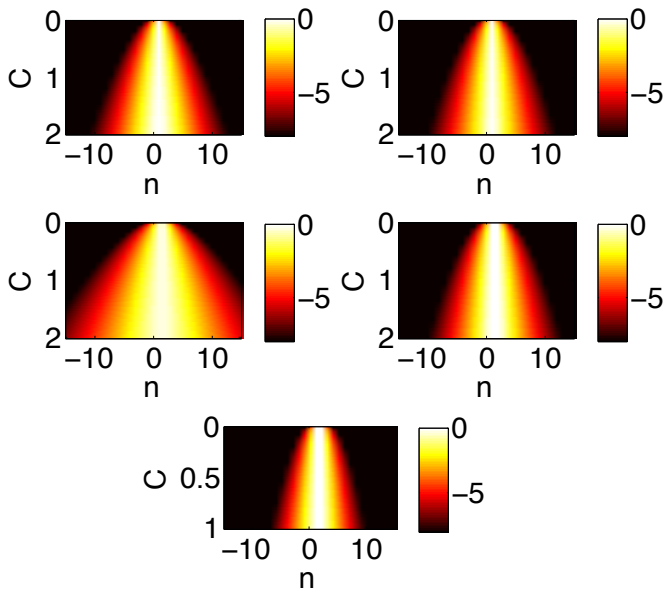


FIG. 2: (Color online) Plots of $\log_{10}(|u_n|^2)$, where u_n at $C = 0$ is given by Eqs. (11) and (12), and at $C > 0$ the soliton solutions u_n are obtained by the continuation in C , see the text. Common parameters are $\gamma = 1$, $\kappa = 1.9$ and $\sigma = 1$. The initial configuration of the excited rungs at $C = 0$ and parameters are: a single in-phase rung with $\delta_1 = \delta_{\text{in}}$, $\Lambda = 2.5$, $N = 40$, $\Delta C = 0.001$ (top left), a single out-of-phase rung with $\delta_1 = \delta_{\text{out}}$, $\Lambda = 2.5$, $N = 40$, $\Delta C = 0.001$ (top right), two in-phase rungs with $\delta_1 = \delta_2 = \delta_{\text{in}}$, $\Lambda = 2$, $N = 80$, $\Delta C = 0.001$ (middle left), two out-of-phase rungs with $\delta_1 = \delta_2 = \delta_{\text{out}}$, $\Lambda = 2.5$, $N = 80$, $\Delta C = 0.001$ (middle right), and, finally, a mixed state carried by two rungs with $\delta_1 = \delta_{\text{in}}$, $\delta_2 = \delta_{\text{out}}$, $\Lambda = 2.5$, $N = 80$, $\Delta C = 0.00001$ (bottom center). Plots of $\log_{10}(|v_n|^2)$ are identical to those of $\log_{10}(|u_n|^2)$. As C increases, small amplitudes appear at adjacent rungs, and the soliton gains width. The corresponding second moment, $w(C)$, defined as per Eq. (18), is shown in Fig. 4. The stability of the solitons shown here is predicted by eigenvalue plots displayed in Fig. 12 for $\gamma = 1$.

Figures 7, 8, 9, 10, 11 are similar to their counterparts 2, 3, 4, 5, 6, respectively, but with the parameters taken as per Eq. (17) instead of Eq. (13). Comparing Figs. 5 and 10 shows that $\sigma = +1$ favors the solutions with in-phase rungs as C increases, while $\sigma = -1$ favors the out-of-phase rungs. In other words, the progressively expanding soliton keeps the in- and out-of-phase structures, in the case of the self-focusing ($\sigma = +1$) and defocusing ($\sigma = -1$) onsite nonlinearity, respectively, in agreement with the well-known principle that discrete solitons feature a staggered pattern in the case of the self-defocusing [22]. Also, according to Eq. (12), for $\sigma = -1$ the asymmetry of the mixed-phase solution is switched in comparison to the $\sigma = +1$ case, lending the in-phase rung a larger magnitude of the fields than in the out-of-phase one.

It is relevant to stress that the discrete solitons seeded in the ACL by double rungs feature a *bi-dimer* structure

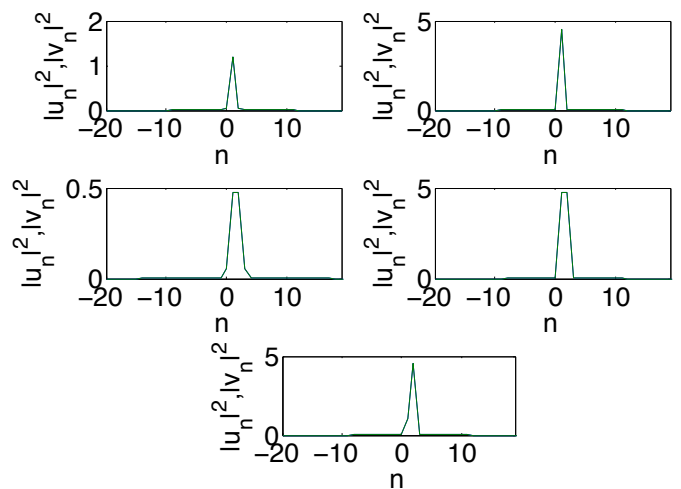


FIG. 3: Profiles of discrete solitons for $C = 0.4$. The configurations of the initial ($C = 0$) solution and other parameters follow the same pattern as in Fig. 2.

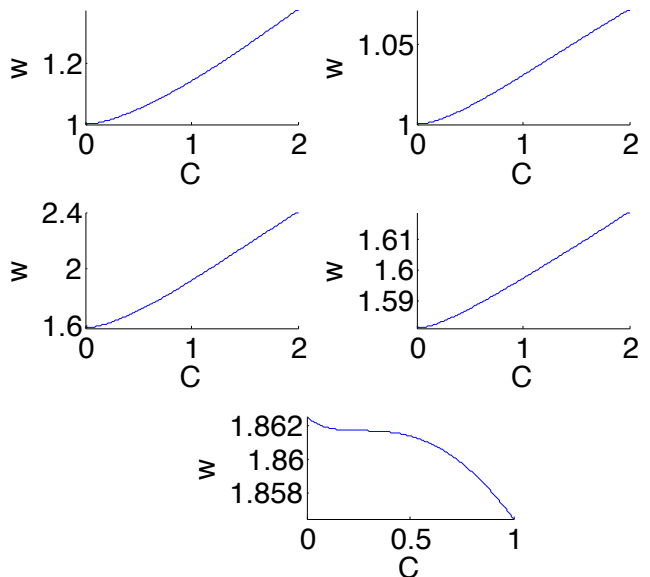


FIG. 4: (Color online) Width diagnostic w , defined as per Eq. (18), corresponding to each of the plots in Fig. 2.

which does not carry a topological charge [20]. I.e., the solitons cannot take the form of vortices, according to our numerical results, (contrary to what is the case, e.g., for a ring containing a single \mathcal{PT} -symmetric dipole [24]).

C. Stability of the discrete solitons

Figure 12 shows two-parameter stability diagrams for the solitons by plotting the largest instability growth rate (if different from zero), $\max(\text{Re}(i\omega))$, as a function of C and γ for parameter values taken per Eq. (13), and Fig. 13 shows the same as per Eq. (17). The respective sta-

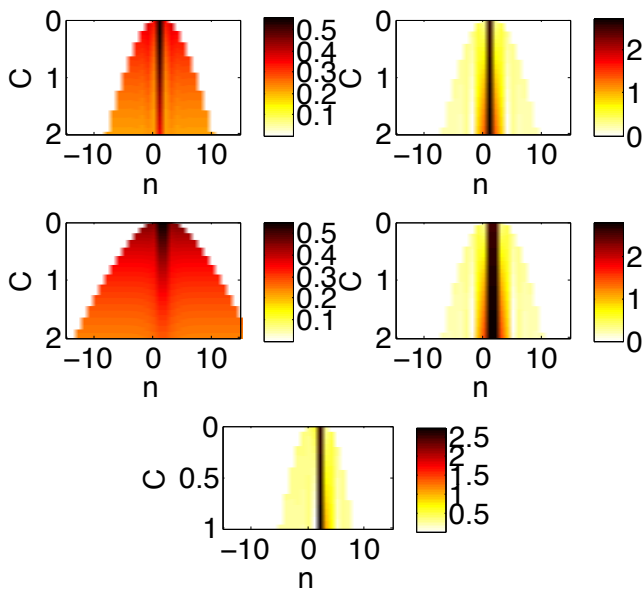


FIG. 5: The phase shift between two edges of the rungs, $|\arg(v_n u_n^*)|$, plotted as a function of C and n , where u is the solution whose absolute value is presented in Fig. 2. The value of $|\arg(v_n u_n^*)|$ is set to zero for any n at which $\log_{10}(|u|^2) \leq -6$ in Fig. 2. In other words, the phase shift is shown as equal to zero when the amplitude is too small. For the top left and middle left plots, the soliton's field is different from zero at one or two in-phase rung(s) when $C = 0$, and as C increases the solutions stay in-phase. For the top right and middle right plots, the field at $C = 0$ is nonzero and out-of-phase at the one or two central rungs, and, as C increases, the fields at these rungs, and at two rungs on either side of the central ones, tend to be out-of-phase, while the field at other rungs, located farther away, tend to be in-phase. Similarly, in the bottom plot, where at $C = 0$ the $n = 1$ rung is in-phase and the $n = 2$ one is out-of-phase, as C increases, most rungs tend to be in-phase, except for $n = 2, 3$.

bility boundaries are shown by green lines (white, in the black-and-white version of the figures). Some comments are relevant here. Recall that Eqs. (9) and (16) impose stability limitations, respectively, from the point of view of the zero-background solution in the former case, and the single-site excitation in the latter case. The former background stability condition indicates that the line of $\gamma = \kappa - C$ (parallel to the antidiagonal cyan line in Fig. 12) poses an upper bound on the potential stability of any excitation, as it is the condition for the stability of the zero background, on top of which any solitary wave is constructed. It can be seen in both Figs. 12 and 13, especially in the right panels of the former and left panels of the latter [where the instability defined by Eq. (16) is less relevant], that the background-instability threshold given by Eq. (9) is an essential stability boundary for the family of the discrete solitons. Of course, additional instabilities due to the localized core part of the solution are possible too, and, as observed in these panels, they somewhat deform the resultant stability region. The ad-

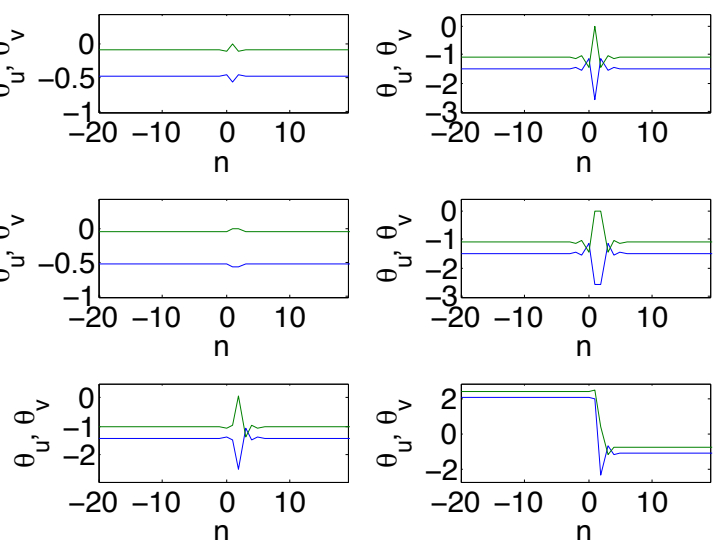


FIG. 6: The phase of each rung, $\theta_u := \arg(u_n)$ (blue) and $\theta_v := \arg(v_n)$ (green) with values in the interval $(-\pi, \pi]$, plotted as a function of the spatial variable n . The top four plots and bottom-most left plot have fixed parameter values $C = 0.4, \gamma = 1$ and $\sigma = 1$. That is, the u_n, v_n solutions for these five plots are the same as those whose modulus is plotted in Fig. 3. In the bottom right plot we show θ_u, θ_v for the same fixed parameter values as the bottom left plot except with $\gamma = 0.8$. The bottom two plots show the different phase profiles that can arise for different γ values, with either same (left) or opposite (right) signs for the phase on the outer portions of the ladder.

ditional instabilities stemming from the excited in-phase rungs in Fig. 12, and their out-of-phase counterparts in Fig. 13, are separately observed in the left panels of the former figure and right panels of the latter one. Given that this critical point was found in the framework of the ACL, it features no C dependence, but it clearly contributes to delimiting the stability boundaries of the discrete solitons; sometimes, this effect is fairly dramatic, as in the middle-row left and right panels of Figs. 12 and 13, respectively, i.e., the two-site, same-phase excitations may be susceptible to this instability mechanism. Although the precise stability thresholds may be fairly complex, arising from the interplay of localized and extended modes in the nonlinear ladder system, a general conclusion is that the above-mentioned instabilities play a critical role for the stability of the localized states in this system (see also the discussion below). Another essential conclusion is that the higher the coupling (C), the less robust the corresponding solutions are likely to be, the destabilization caused by the increase of C being sometimes fairly dramatic.

The values of $i\omega$ whose maximum real part is represented in Figs. 12 and 13 were computed with the help of an appropriate numerical eigenvalue solver. At $C = 0$, the eigenvalues agree with Eqs. (14) and (15). As shown in Figs. 14 and 15, following the variation of C and γ ,

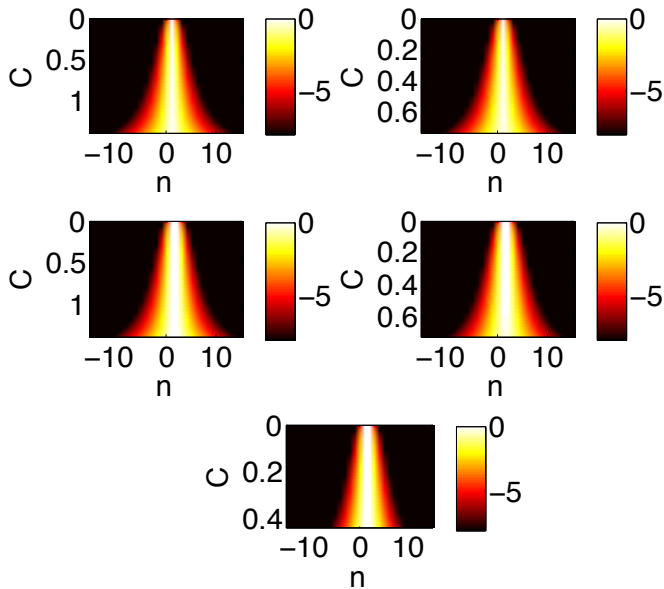


FIG. 7: (Color online) The same as Fig. 2, but for $\sigma = -1$. Common parameters are $\kappa = 2$ and $\gamma = 1$. The initial values of δ_1 and δ_2 at $C = 0$ follow the pattern of Fig. 2. Other parameters are: $\Lambda = 5, N = 80, \Delta C = 0.001$ on the top left, $\Lambda = 3.5, N = 80, \Delta C = 0.001$ on the top right, $\Lambda = 5, N = 80, \Delta C = 0.001$ on the middle left, $\Lambda = 3.5, N = 40, \Delta C = 0.001$ on the middle right, and finally $\Lambda = 3.085, N = 40, \Delta C = 0.0001$ on the bottom center. As C increases, small amplitudes appear at adjacent sites, and the soliton gains width, as shown by means of w in Fig. 9. The stability of the solitons shown here is predicted by the eigenvalue plots in Fig. 13 at $\gamma = 1$.

eigenvalues (14), associated with the empty (zero-value) sites, vary in accordance with the prediction of Eq. (8), and eigenvalues (15), associated with excited rungs, also shift in the complex plane upon variation of C, γ . In the case of the mixed-phase solutions with asymmetric amplitude (seen in the bottom-most plot of Fig. 3), there is a stable region for low values of the parameters C and γ . For larger values of γ there are parametric intervals (across $C > 0$ for fixed γ) in which discrete solitons with phase profiles different from those initialized in the ACL of $C = 0$ have been identified; see the bottom two plots in Fig. 6. These distinct branches of the unstable solutions give rise to “streaks” observed in the bottom middle panel of Fig. 12. The amplitude profiles of such alternate solutions are similar to those shown in the bottom plot of Fig. 3, and the gain in width function defined in (18) as a function of C is similar to the examples shown in the bottom plots of Figs. 2, 4. Mechanisms by which solutions become unstable for these alternate solutions are outlined below.

The most obvious type of the instability is associated with initializing a solution at $C = 0$ from a single unstable rung, i.e., at $\gamma > \gamma_{cr}^{(2)}(C = 0)$ in (16). Eigenvalues for this type of the instability are shown in the top two panels of Fig. 15. There are three other scenarios of

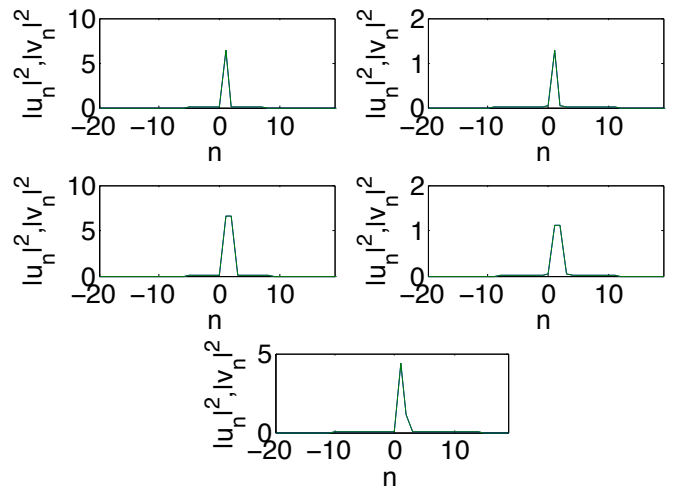


FIG. 8: Profiles of the discrete solitons at $C = 0.4$, for $\sigma = -1$. The configurations of the initial $C = 0$ solution and parameters follow the same pattern as in Fig. 7.

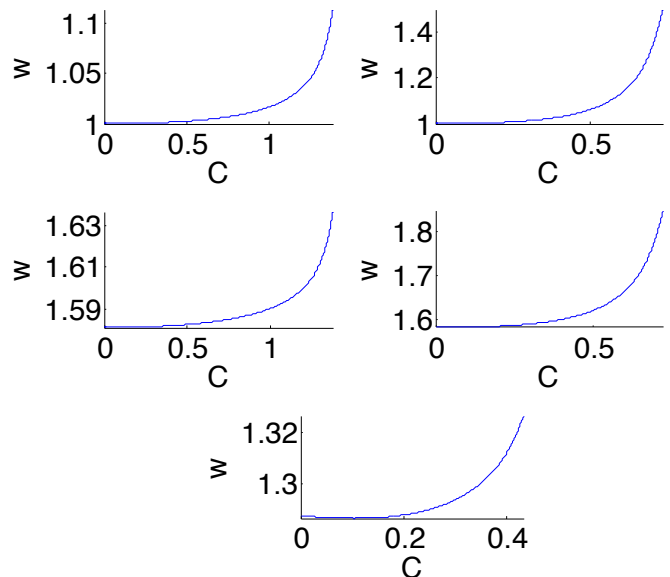


FIG. 9: (Color online) The width diagnostic of the discrete solitons, defined as per Eq. (18), corresponding to each of the plots in Fig. 7.

destabilization of the discrete solitons with the increase of C , each corresponding to a particular type of a critical point (transition to the instability). These transitions are demonstrated in Figs. 14-15. The first type occurs when eigenvalue ω associated with an excited rung collides with one of the intervals in Eq. (10). This weak instability generates an eigenfrequency quartet and is represented in Figs. 12 and 13, where the green boundary deviates (as C increases from 0) from the threshold given by Eq. (16). Figures 14 and 15 illustrate this type of transition in more detail by plotting the eigenvalues directly in the complex plane.

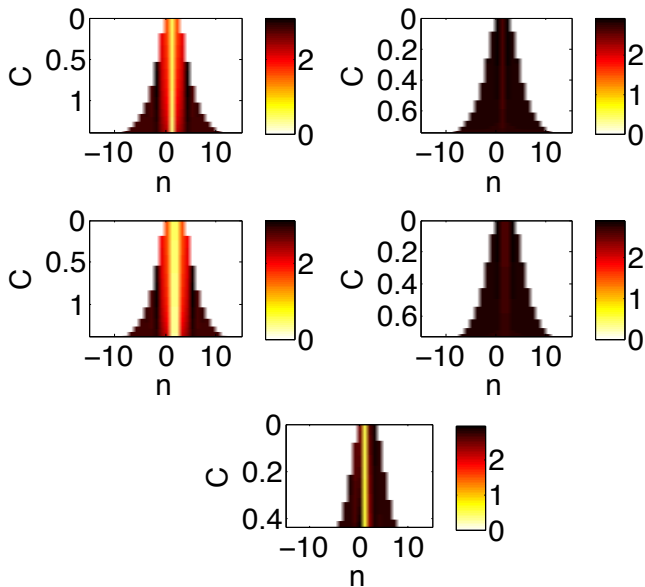


FIG. 10: (Color online) The same as Fig. 5 but for $\sigma = -1$, i.e., for the discrete solitons presented in Fig. 7. For the top left and middle left plots, the soliton's field is nonzero at one or two in-phase rung(s) when $C = 0$, and as C increases these rungs remain in-phase, while all the others are out-of-phase. For the top right and middle right plots, the soliton's field at $C = 0$ is nonzero and out-of-phase at one or two central rungs, and all rungs remain out-of-phase with the increase of C . In the bottom plot, only the $n = 1$ rung remains in-phase, while all others are out-of-phase.

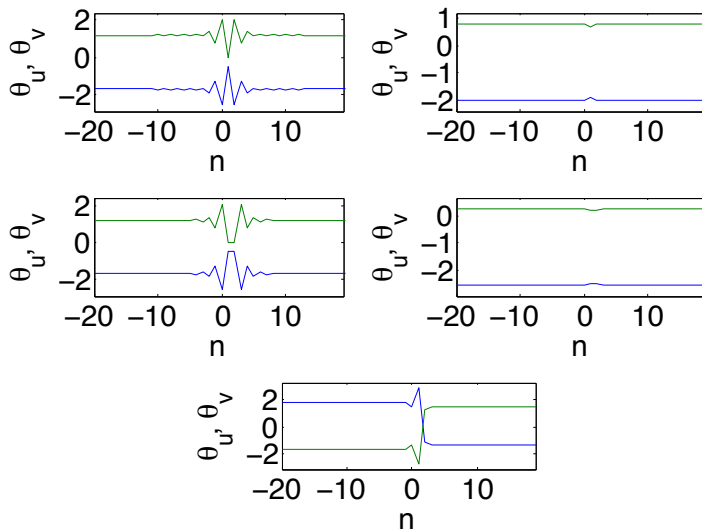


FIG. 11: The phase of each rung, $\theta_u := \arg(u_n)$ (blue) and $\theta_v := \arg(v_n)$ (green) in the interval $(-\pi, \pi]$, plotted as a function of the spatial variable n for the fixed parameter values $C = 0.4, \gamma = 1$ and $\sigma = -1$. That is, the u_n, v_n solutions are the same as those whose modulus is plotted in Fig. 8.

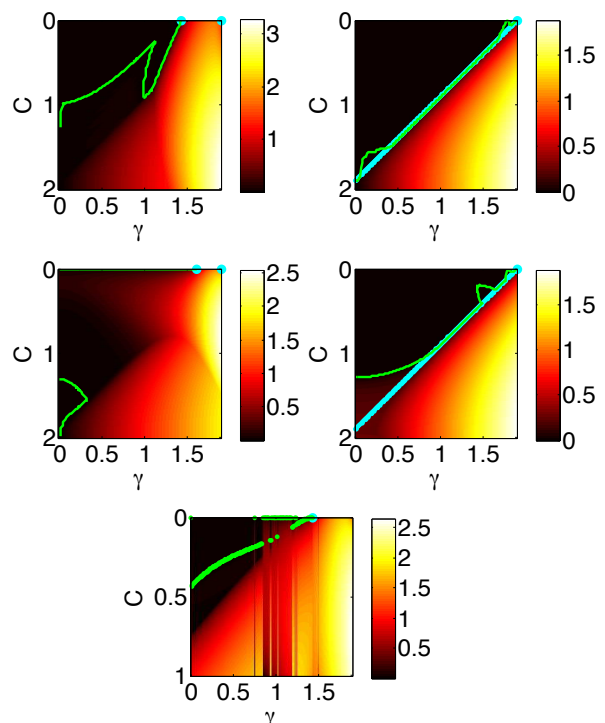


FIG. 12: (Color online) The largest instability growth rate, $\max(\text{Re}(i\omega))$, determined by matrix M in Eq. (5), for parameter values following the same pattern as in Fig. 2, except that here γ varies along the horizontal axis. In the top two plots in the right column, the cyan line represents the analytically predicted critical value, $\gamma_{\text{cr}}^{(1)}(C) = \kappa - C$; this line originates from the cyan dot in the corner at $\gamma_{\text{cr}}^{(1)}(0) = \kappa$, see Eq. (9). If an in-phase excited rung is present, then the second cyan dot is located at $\gamma_{\text{cr}}^{(2)} = \sqrt{\kappa^2 - \Lambda^2/4}$, in accordance with Eq. (16). Green lines indicate stability boundaries, between the dark region corresponding to stability [or very weak instability, with $\max(\text{Re}(i\omega)) < 10^{-3}$], and the bright region corresponding to the instability.

The second type of the transition occurs when the intervals in Eq. (10) come to overlap at $\gamma = \gamma_{\text{cr}}^{(1)}(C)$, see Eq. (9). This is the background instability at empty sites, as shown in Figs. 12 and 13 by bright spots originating from the corners of the diagrams, where $\gamma = \kappa = \gamma_{\text{cr}}^{(1)}(C = 0)$. A more detailed plot of these eigenvalues and the corresponding collisions in the complex eigenvalue plane is displayed in Fig. 14.

The third type of the instability onset occurs for essentially all values of C in the case of two in-phase rungs at $\sigma > 0$, or two out-of-phase ones at $\sigma < 0$. It may be thought of as a localized instability due to the simultaneous presence of two potentially unstable elements, due to the instability determined by Eq. (16). At $C > 0$, it is seen as the bright spots in Figs. 12 and 13 originating from $\gamma_{\text{cr}}^{(2)}(C = 0) = \sqrt{\kappa^2 - \Lambda^2/4}$. The eigenvalues emerge from the corresponding zero eigenvalues at $C = 0$. That is, in the middle-left plot of Fig. 12 at $C = 0$ for $\gamma < \gamma_{\text{cr}}^{(2)}(C = 0)$ there are four zero eigenvalues; as C increases, two of the four eigenvalues move from zero

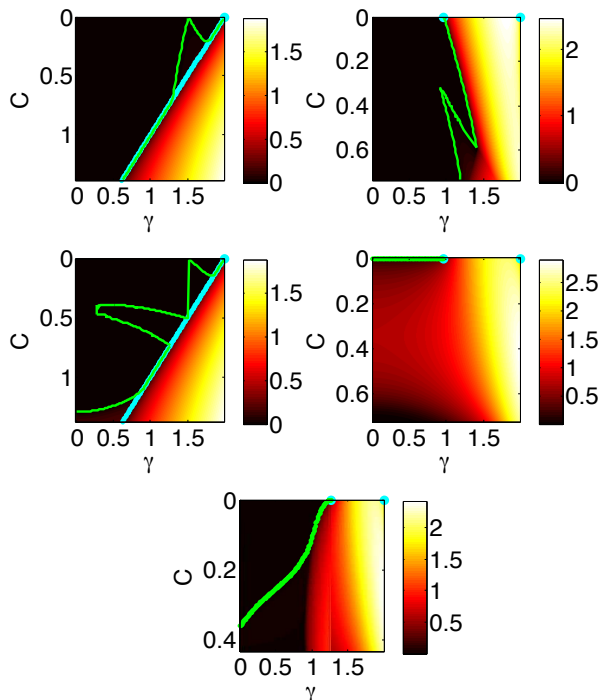


FIG. 13: (Color online) The same as in Fig. 12, but for parameter values from Fig. 7. Here the cyan line is drawn on the top two plots in the left column, and the second cyan dot on the $C = 0$ axis appears only in the case where the out-of-phase excited rung is present at $C = 0$.

onto the real axis in the complex plane. A similar effect is observed at $\gamma < \gamma_{\text{cr}}^{(2)}(C = 0)$ in the middle-row right plot of Fig. 13.

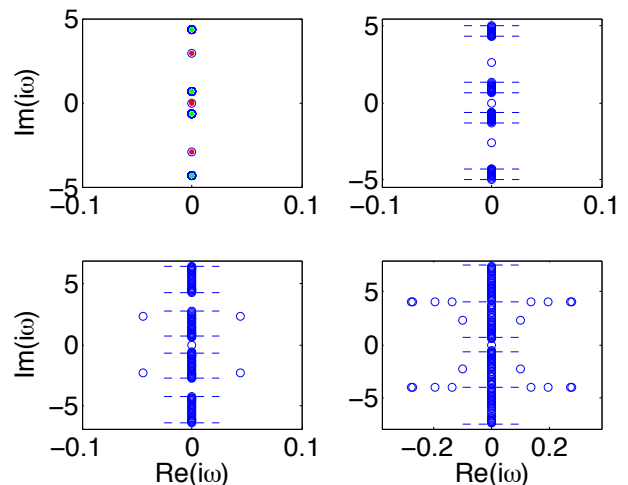
Finally, it is worth making one more observation in connection, e.g., to Fig. 15 and the associated jagged lines in the top right panel of Fig. 13. Notice that, as C increases, initial stabilization of the mode unstable due to the criterion given by Eq. (16) takes place, but then a collision with the continuous spectrum on the imaginary axis provides destabilization anew. It is this cascade of events that accounts for the jaggedness of the curve in the top right of Fig. 13 and in similar occurrences (e.g., in the top left plot of Fig. 12). We add this explanation to the set of possible instabilities discussed above, to explain the complex form of the stability boundaries featured by our two-dimensional plots.

D. The evolution of discrete solitons

To verify the above predictions for the stability of the discrete solitons, we simulated evolution of the perturbed solutions in the framework of Eq. (1) by means of the standard Runge-Kutta fourth-order integration scheme. In Figs. 16, 17, and 18 we display examples of the evolution of each of the three instability types which were identified in Section III B.

For the first type, when the instability arises from

FIG. 14: (Color online) Stability eigenvalues $i\omega$ in the complex plane, for parameters chosen in accordance with the top-most left panel of Fig. 12 with $\gamma = 0.5$. For $C = 0$, in the top left plot we show the agreement of the numerically found eigenvalues (blue circles) with results produced by Eqs. (14) (green filled circles) and (15) (red filled). For $C = 0.3$, in the top right panel we show that the eigenvalues associated with the zero solution indeed lie within the predicted intervals (10), the boundaries of which are shown by dashed lines. Next, for $C = 1$, in the bottom left plot we observe that values of $i\omega$ associated with the excited state have previously (at smaller C) merged with the dashed intervals, and now an unstable quartet has emerged from the axis. For $C = 1.5$, in the bottom right panel the critical point corresponding to Eq. (9) is represented, where unstable eigenvalues emerge from the axis at the values of $\pm(\Lambda + C)$, as the intervals in Eq. (10) merge. Comparing plots in the bottom row, we conclude that the critical point of the latter type gives rise, in general, to a stronger instability than the former one.

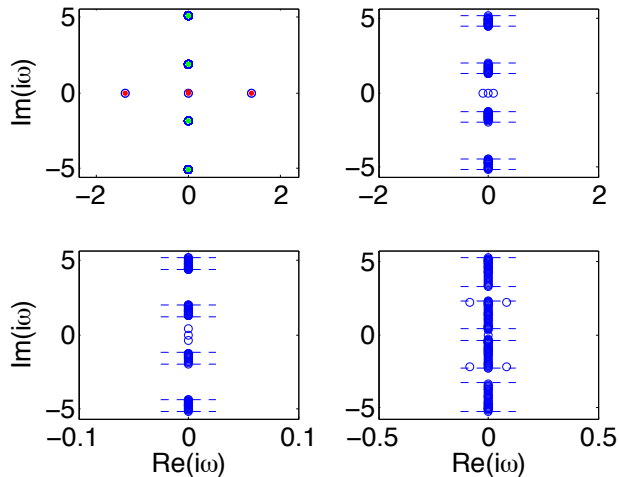


the collision of eigenvalues associated with the excited and empty rungs, the corresponding unstable eigenmode arises in the form of a quartet of eigenfrequencies. In Fig. 16 we demonstrate that this instability leads to the growth of the solution amplitudes and oscillations at the central rung. The corresponding (chiefly localized, although with a weakly decaying tail) instability eigenvectors are shown in the top panels of the figure, while the bottom panels show how the initial conditions evolve in time through the oscillatory growth, in accordance with the presence of the unstable complex eigenfrequencies.

For the second type of the instability, which arises from the collision of eigenvalues in intervals (10), which are all associated with empty rungs, the corresponding unstable eigenmode is delocalized. It is shown in Fig. 17 that the corresponding unstable soliton does not preserve its shape. Instead, the instability causes delocalization of the solution, which acquires a tail reminiscent of the spatial profile of the corresponding unstable eigenvector.

Lastly, the third type of the instability is shown in Fig. 18. It displays the case of two excited in-phase rungs at $\sigma = 1$. Other examples of the same type are

FIG. 15: (Color online) The same as in Fig. 14, but for parameters chosen in accordance with the top right panel of Fig. 13, with $\gamma = 1.2$. At $C = 0$, in the top left plot we show the agreement of the numerically found eigenvalues (blue circles) with Eqs. (14) (green filled circles) and (15) (red filled). At $C = 0.275$, in the top right we see that eigenvalues associated to the red x's have moved inward towards zero. Next, for $C = 0.3$, in the bottom left panel we observe that, after merging with zero, the eigenvalues now emerge from zero on the imaginary axis. Finally, at $C = 0.7$ in the bottom right panel, we observe that, after the eigenvalues merge with the dashed-line intervals, an unstable quartet emerges from the axis.



similar – e.g., with two out-of-phase excited rungs at $\sigma = -1$. The instability has a localized manifestation with the amplitudes growing at the gain nodes of each rung and decaying at the loss ones.

IV. CONCLUSIONS

We have introduced the lattice of the ladder type with staggered pairs of mutually compensated gain and loss elements at each rung, and the usual onsite cubic non-linearity, self-focusing or defocusing. This nearly-one-dimensional system is the simplest one which features *two-dimensional* \mathcal{PT} symmetry. It may be realized in optics as a waveguide array. We have constructed families of discrete stationary solitons seeded by a single excited rung, or a pair of adjacent ones, in the anti-continuum limit of uncoupled rungs. The seed excitations may have the in-phase or out-of-phase structure in the vertical direction (between the gain and loss poles). The double seed with the in- and out-of-phase structures in the two rungs naturally features an asymmetric amplitude profile. We have identified the stability of the discrete solitons via the calculation of eigenfrequencies for small per-

turbations, across the system's parameter space. A part of the soliton families are found to be dynamically stable, while unstable solitons exhibit three distinct scenarios of the evolution. The different scenarios stem, roughly, from

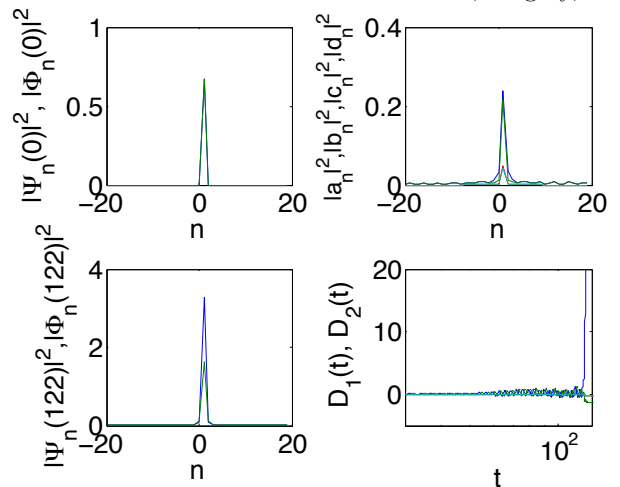


FIG. 16: (Color online) The evolution of the soliton whose instability is predicted in the top-most left panel of Fig. 12 for $C = 1$ and $\gamma = 0.5$. The complex plane of all the eigenvalues for this solution is shown in the bottom left plot of Fig. 14. The top right plot shows the squared absolute values of perturbation amplitudes a_n, c_n (higher amplitudes) and b_n, d_n (lower amplitudes), defined in Eq. (4). The top left plot shows the solution at $t = 0$, and the bottom left plot shows the solution at $t = 122$ with $|\Psi_n(t = 122)|^2$ in blue and $|\Phi_n(t = 122)|^2$ in green. In the course of the evolution, the soliton maintains its shape, while the amplitude at the central rung ($n = 1$) grows with oscillations; the growth on the gain side, associated to Ψ_n , is ultimately dominant. Quantities $D_1(t) \equiv |\Psi_1(t)|^2 - |\Psi_1(0)|^2$ and $D_2(t) \equiv |\Phi_1(t)|^2 - |\Phi_1(0)|^2$ are shown in the bottom right plot, in order to better demonstrate the growing oscillations.

interactions of localized modes with extended ones, from extended modes alone, or from localized modes alone.

A natural extension of the work may be the consideration of mobility of kicked discrete solitons in the present ladder system. It may also be interesting to seek nonstationary solitons with periodic intrinsic switching, cf. Ref. [25]. A challenging perspective is the development of a 2D extension of the system. Effectively, this would entail adding further alternating ladder pairs along the transverse direction and examining 2D discrete configurations. It may be relevant in such 2D extensions to consider different lattice settings that support not only solutions in the form of discrete solitary waves but also ones built as discrete vortices, similarly to what has been earlier done in the DNLS system [22], and recently in another 2D \mathcal{PT} -symmetric system [18].

[1] D. N. Christodoulides, F. Lederer and Y. Silberberg, “Discretizing light behaviour in linear and nonlinear

waveguide lattices, Nature **424**, 817-823 (2003); F. Led-

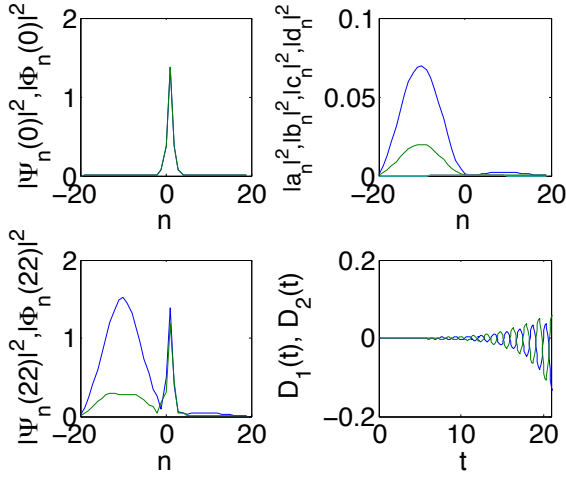


FIG. 17: (Color online) The evolution of the discrete soliton whose instability is predicted is in the top-most left panel of Fig. 12 for $C = 1.5$ and $\gamma = 0.5$. The complex plane of all the eigenvalues for this solution is shown in the bottom right plot of Fig. 14. The top right plot has the same meaning as in Fig. 16, where here $|b_n|^2, |d_n|^2$ are mostly zero while $|a_n|^2, |c_n|^2$ have nonzero amplitudes. In the course of the evolution the soliton does not maintain its shape. In particular, the solution profiles at $t = 22$ are shown in the left panel at the bottom bearing the apparent signature of the delocalized, unstable eigenmode; the delocalization is stronger in the Ψ solution associated with gain. Similar to Fig. 16 we plot $D_1(t), D_2(t)$ in the bottom right plot. This plot shows that the central node experiences oscillations similar to Fig. 16 but the oscillatory effect is dominated by the delocalization seen in the bottom left plot, which grows and exceeds past the shorter peaks in the center.

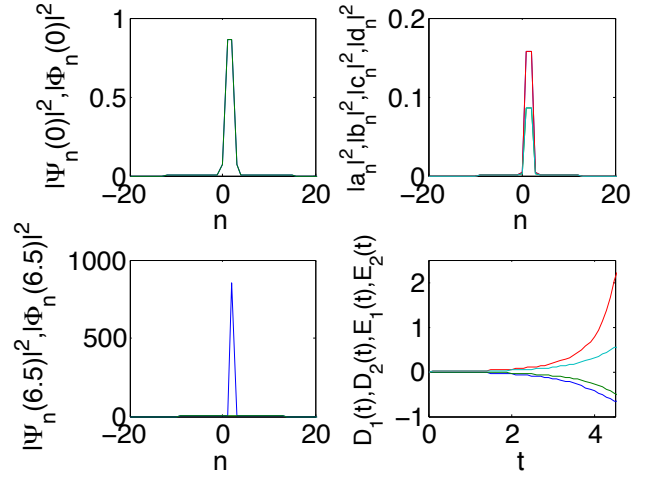


FIG. 18: (Color online) The evolution of the solitary wave whose instability is predicted is in the middle left panel of Fig. 12 for $C = 0.5$ and $\gamma = 1.5$. The complex plane including all the eigenvalues for this solution is similar to the top right plot in Fig. 15. The top right plot here shows the squared absolute values of perturbation amplitudes a_n, b_n (lower amplitudes) and c_n, d_n (higher amplitudes) defined in Eq. (4). The top left plot shows the solution at $t = 0$, and the bottom left plot shows the solution at $t = 6.5$ with $|\Psi_n(6.5)|^2$ in blue and $|\Phi_n(6.5)|^2$ in green. In the course of the evolution, the soliton maintains its shape, while the amplitude at the rung $n = 2$ grows with weak oscillations and with higher growth on the Ψ side associated with gain. Quantities $D_1(t) \equiv |\Psi_1(t)|^2 - |\Psi_1(0)|^2$ (blue), $D_2(t) \equiv |\Phi_1(t)|^2 - |\Phi_1(0)|^2$ (green), $E_1(t) \equiv |\Psi_2(t)|^2 - |\Psi_2(0)|^2$ (cyan) and $E_2(t) \equiv |\Phi_2(t)|^2 - |\Phi_2(0)|^2$ (red) are shown in the bottom right plot to highlight the growth.

erer, G. I. Stegeman,, D. N. Christodoulides, G. Assanto, M. Segev and Y. Silberberg, “Discrete solitons in optics,” *Phys. Rep.* **463**, 1-126 (2008); I. L. Garanovich, S. Longhi, A. A. Sukhorukov, and Y. S. Kivshar, “Light propagation and localization in modulated photonic lattices and waveguides,” *Phys. Rep.* **518**, 1-79 (2012); Z. Chen, M. Segev and D. N. Christodoulides, “Optical spatial solitons: historical overview and recent advances,” *Rep. Prog. Phys.* **75**, 086401 (2012).

- [2] B. A. Malomed and P. G. Kevrekidis, “Discrete vortex solitons,” *Phys. Rev. E* **64**, 026601 (2001); P. G. Kevrekidis, B. A. Malomed, and Yu. B. Gaididei, “Solitons in triangular and honeycomb dynamical lattices with the cubic nonlinearity,” *Phys. Rev. E* **66**, 016609 (2002); P. G. Kevrekidis, B. A. Malomed, Z. Chen, and D. J. Frantzeskakis, “Stable higher-order vortices and quasivortices in the discrete nonlinear Schrödinger equation,” *Phys. Rev. E* **70**, 056612 (2004); M. Öster and M. Johansson, “Stable stationary and quasiperiodic discrete vortex breathers with topological charge $S=2$,” *Phys. Rev. E* **73**, 066608 (2006); Mejía-Cortés, J. M. Soto-Crespo, M. I. Molina, and R. Vicencio, “Dissipative vortex solitons in two-dimensional lattices,” *Phys. Rev. A* **82**, 063818 (2010).
- [3] D. Neshev, T. J. Alexander, E. A. Ostrovskaya, Y. S. Kivshar, H. Martin, I. Makasyuk, and Z. Chen, “Ob-

ervation of discrete vortex solitons in optically induced photonic lattices,” *Phys. Rev. Lett.* **92**, 123903 (2004); J. W. Fleischer, G. Bartal, O. Cohen, O. Manela, M. Segev, J. Hudock, and D. N. Christodoulides, “Observation of vortex-ring discrete solitons in 2D photonic lattices,” *Phys. Rev. Lett.* **92**, 123904 (2004); B. Terhalle, T. Richter, A. S. Desyatnikov, D. N. Neshev, W. Królikowski, F. Kaiser, C. Denz, and Y. S. Kivshar, “Observation of multivortex solitons in photonic lattices,” *Phys. Rev. Lett.* **101**, 013903 (2008).

- [4] D. N. Christodoulides and E. D. Eugenieva, “Blocking and routing discrete solitons in two-dimensional networks of nonlinear waveguide arrays,” *Phys. Rev. Lett.* **87**, 233901(2001).
- [5] N. K. Efremidis, S. Sears, D. N. Christodoulides, J. W. Fleischer, and M. Segev, “Discrete solitons in photorefractive optically induced photonic lattices,” *Phys. Rev. E* **66**, 046602 (2002); J. W. Fleischer, M. Segev, N. K. Efremidis, and D. N. Christodoulides, “Observation of two-dimensional discrete solitons in optically induced nonlinear photonic lattices,” *Nature* **422**, 147-150 (2003).
- [6] A. A. Sukhorukov, Y. S. Kivshar, H. S. Eisenberg, and Y. Silberberg, “Spatial optical solitons in waveguide arrays,” *IEEE J. Quantum Electron.* **39**, 31-50 (2003); A. Szameit, J. Burghoff, T. Pertsch, S. Nolte, A. Tünnermann, and F. Lederer, “Two-dimensional soliton in cubic fs laser written waveguide arrays in fused silica,” *Opt. Exp.* **14**,

- 6055-6062 (2006); A. Szameit and S. Nolte, “Discrete optics in femtosecond-laser-written photonic structures,” *J. Phys. B: At. Mol. Opt. Phys.* **43**, 163001 (2010).
- [7] T. Schwartz, G. Bartal, S. Fishman, and M. Segev, “Transport and Anderson localization in disordered two-dimensional photonic lattices,” *Nature* **446**, 52-55 (2007); Y. Lahini, A. Avidan, F. Pozzi, M. Sorel, R. Morandotti, D. N. Christodoulides, and Y. Silberberg, “Anderson localization and nonlinearity in one-dimensional disordered photonic lattices,” *Phys. Rev. Lett.* **100**, 013906 (2008).
- [8] A. Ruschhaupt, F. Delgado, and J. G. Muga, “Physical realization of \mathcal{PT} -symmetric potential scattering in a planar slab waveguide,” *J. Phys. A* **38**, L171-L176 (2005); K. G. Makris, R. El-Ganainy, D. N. Christodoulides, and Z. H. Musslimani, “Beam Dynamics in \mathcal{PT} Symmetric Optical Lattices,” *Phys. Rev. Lett.* **100**, 103904 (2008); S. Longhi, “Spectral singularities and Bragg scattering in complex crystals,” *Phys. Rev. A* **81**, 022102 (2010); C. E. Rüter, K. G. Makris, R. El-Ganainy, D. N. Christodoulides, M. Segev, and D. Kip, “Observation of parity-time symmetry in optics,” *Nature Phys.* **6**, 192-195 (2010); K. G. Makris, R. El-Ganainy, D. N. Christodoulides, and Z. H. Musslimani, “ \mathcal{PT} symmetric periodic optical potentials,” *Int. J. Theor. Phys.* **50**, 1019-1041 (2011).
- [9] R. Driben and B. A. Malomed, Stability of solitons in parity-time-symmetric couplers, *Opt. Lett.* **36**, 4323-4325 (2011); N. V. Alexeeva, I. V. Barashenkov, A. A. Sukhorukov, and Y. S. Kivshar, Optical solitons in \mathcal{PT} -symmetric nonlinear couplers with gain and loss *Phys. Rev. A* **85**, 063837 (2012); Yu. V. Bludov, R. Driben, V. V. Konotop, and B. A. Malomed, “Instabilities, solitons and rogue waves in \mathcal{PT} -coupled nonlinear waveguides”, *J. Opt.* **15**, 064010 (2013).
- [10] A. E. Miroshnichenko, B. A. Malomed, and Y. S. Kivshar, “Nonlinearly \mathcal{PT} -symmetric systems: Spontaneous symmetry breaking and transmission resonances”, *Phys. Rev. A* **84**, 012123 (2011); S. V. Dmitriev, S. V. Suchkov, A. A. Sukhorukov, and Y. S. Kivshar, “Scattering of linear and nonlinear waves in a waveguide array with a \mathcal{PT} -symmetric defect,” *ibid.* **84**, 013833 (2011); S. V. Suchkov, A. A. Sukhorukov, S. V. Dmitriev, and Y. S. Kivshar, “Scattering of the discrete solitons on the \mathcal{PT} -symmetric defects,” *EPL* **100**, 54003 (2012); A. Regensburger, M. A. Miri, C. Bersch, and J. Näger, “Observation of defect states in \mathcal{PT} -symmetric optical lattices,” *Phys. Rev. Lett.* **110**, 223902 (2013).
- [11] J. D’Ambroise, P. G. Kevrekidis, and S. Lepri, “Asymmetric Wave Propagation Through Nonlinear \mathcal{PT} -symmetric Oligomers”, *J. Phys. A* **45**, 444012 (2012); J. D’Ambroise, P. G. Kevrekidis, and S. Lepri, “Eigenstates and instabilities of chains with embedded defects”, *Chaos* **23**, 023109, 10 pages (2013).
- [12] W. H. Weber and G. W. Ford, “Propagation of optical excitations by dipolar interactions in metal nanoparticle chains” *Phys. Rev. B* **70**, 125429 (2004); P. A. Belov and C. R. Simovski, “Homogenization of electromagnetic crystals formed by uniaxial resonant scatterers” *Phys. Rev. E* **72**, 026615 (2005); I.V. Shadrivov, A.A. Zharov, N.A. Zharova, Yu.S. Kivshar, “Nonlinear magnetoinductive waves and domain walls in composite metamaterials”, *Photonics and Nanostructures – Fundamentals and Applications* **4**, 69 (2006); R.E. Noskov, P.A. Belov and Yu.S. Kivshar, “Subwavelength Modulational Instability and Plasmon Oscillons in Nanoparticle Arrays” *Phys. Rev. Lett.* **108**, 093901 (2012).
- [13] X. Zhang, J. Chai, J. Huang, Z. Chen, Y. Li, and B. A. Malomed, “Discrete solitons and scattering of lattice waves in guiding arrays with a nonlinear \mathcal{PT} -symmetric defect, *Opt. Exp.* **22**, 13927-13939 (2014).
- [14] K. Li and P. G. Kevrekidis “ \mathcal{PT} -symmetric oligomers: Analytical solutions, linear stability and nonlinear dynamics”, *Phys. Rev. E* **83**, 066608 (2011). D. A. Zezyulin, and V. V. Konotop, “Nonlinear Modes in Finite-Dimensional \mathcal{PT} -Symmetric Systems,” *Phys. Rev. Lett.* **108**, 213906 (2012).
- [15] Y. V. Kartashov, B. A. Malomed, and L. Torner, “Unbreakable \mathcal{PT} symmetry of solitons supported by inhomogeneous defocusing nonlinearity”, *Opt. Lett.* **39**, 5641-5644 (2014).
- [16] S. V. Suchkov, B. A. Malomed, S. V. Dmitriev, and Y. S. Kivshar, “Solitons in a chain of \mathcal{PT} -invariant dimers”, *Phys. Rev. E* **84**, 046609 (2011).
- [17] S. V. Suchkov, S. V. Dmitriev, B. A. Malomed, and Y. S. Kivshar, “Wave scattering on a domain wall in a chain of \mathcal{PT} -symmetric couplers”, *Phys. Rev. A* **85**, 033835 (2012).
- [18] Z. Chen, J. Liu, S. Fu, Y. Li, and B. A. Malomed, “Discrete solitons and vortices on two-dimensional lattices of \mathcal{PT} -symmetric couplers”, *Opt. Exp.* **22**, 29679-29692 (2014).
- [19] K. Li, P. G. Kevrekidis, B. A. Malomed, and U. Günther, “Nonlinear \mathcal{PT} -symmetric plaquettes”, *J. Phys. A* **45**, 444021 (2012).
- [20] K. Li, P. G. Kevrekidis, and B. A. Malomed, “Nonlinear modes and symmetries in linearly-coupled pairs of \mathcal{PT} -invariant dimers”, *Stud. Appl. Math.* **133**, 281-297 (2014).
- [21] I. Szelenowicz, M. A. Hasan, Y. Starosvetsky, A. Vakakis, and C. Daraio, “Energy equipartition in two-dimensional granular crystals with spherical intruders”, *Phys. Rev. E* **87**, 032204 (2013).
- [22] P. G. Kevrekidis, *The Discrete Nonlinear Schrödinger Equation: Mathematical Analysis, Numerical Computations, and Physical Perspectives* (Springer: Berlin and Heidelberg, 2009).
- [23] T. J. Alexander, A. A. Sukhorukov, Yu. S. Kivshar, Asymmetric vortex solitons in nonlinear periodic lattices, *Phys. Rev. Lett.* **93**, 063901 (2004).
- [24] D. Leykam, V. V. Konotop, and A. S. Desyatnikov, “Discrete vortex solitons and parity time symmetry”, *Opt. Lett.* **38**, 371-373 (2013).
- [25] A. S. Desyatnikov, M. R. Dennis, and A. Ferrando, All-optical discrete vortex switch, *Phys. Rev. A* **83**, 063822 (2011).